Evolution of magma decompression and discharge during a Plinian event (Late Bronze-Age eruption, Santorini) from multiple eruption-intensity proxies

Madison Myers, Timothy H. Druitt, Federica Schiavi, Lucia Gurioli, Taya Flaherty

Evolution of magma ascent and discharge during a Plinian event (Late Bronze-Age eruption, Santorini) from multiple eruption-intensity proxies

Madison L. Myers[a,b], Timothy H. Druitt[a], Federica Schiavi[a], Lucia Gurioli[a], and Taya Flaherty[a]

[a] Université Clermont Auvergne, CNRS, IRD, OPGC, Laboratoire Magmas et Volcans, F-63000 Clermont-Ferrand, France

[b] Montana State University, Department of Earth Sciences, Bozeman MT 59717-1272

*Corresponding author. Email address: madison.myers@montana.edu

Abstract

We have coupled three independent methods to investigate the time-evolution of eruptive intensity during the sub-Plinian and Plinian phases of the 3600 y BP Late Bronze Age eruption of Santorini Volcano: (1) mass eruption rate based on new lithic isopleth maps for multiple layers of the fall deposit, (2) magma decompression rate calculated from vesicle number densities, and (3) magma decompression rate calculated from H_2O gradients in melt reentrants, with methods 2 and 3 measured on the same suite of pyroclasts. Mass eruption rate increased by two orders of magnitude, reaching 210×10^6 kg s^{-1} at the peak of the Plinian phase (plume height 28.4 ± 1.0 km); it then declined in the final stage of fallout emplacement following the first generation of pyroclastic surges. Decompression rates from melt reentrants (0.008 to 0.25 MPa s^{-1}) are two to three orders of magnitude lower than those from vesicle number densities, assuming heterogeneous vesicle nucleation (2 to 19 MPa s^{-1}). Melt reentrants probably record slow decompression in the deep feeder conduit, whereas vesicles record much higher rates of decompression in the shallow conduit due to the steep, non-linear pressure gradients associated with magma vesiculation and fragmentation. Upwardly converging flow from a dike-like, deep conduit to a more cylindrical, shallow conduit may also have played a role in causing upwardly accelerating flow. Variations in deep decompression rate recorded by melt reentrants are decoupled from mass eruption rate, whereas those recorded by vesicles lie in between. Taken with the transition from unsteady to steady Plinian eruption conditions, this may reflect the existence of transient flow conditions in the conduit system due to progressing widening and lengthening of a deep feeder dike as Plinian eruption progressed. As the mass eruption rate rose to its peak value, the fragmentation level fell in the conduit due to increasing rates of magma strain and decompression.

Keywords: Plinian eruption, Santorini, decompression rate, conduit development, vesicle number density, melt reentrant

Introduction

Caldera-forming explosive eruptions are amongst the most devastating natural events on Earth **(Mason et al. 2004; Miller and Wark 2008).** As more than 500 million people live within the maximum exposure range of a volcano (**Doocy et. al 2013**), refining techniques to measure how quickly magma moves to the surface, and how magma flow evolves over the course of an eruption, is crucial for improved hazards monitoring and risk mitigation. Determining the processes that control transitions in eruption style, which commonly take place during eruptions due to shifts in external and internal parameters, is also important **(Hildreth and Drake 1992; Woods and Koyaguchi 1994; Castro and Gardner 2008; Degruyter et al. 2012)**. Few silicic caldera-forming eruptions have ever been recorded by modern scientific instrumentation, so understanding of the processes leading up to, and during, such eruptions relies heavily on studies of their erupted products.

Three main clast-based techniques are available for estimating magma flow rate from measurements on pyroclastic fall deposits. One uses clast-isopleth data to estimate eruption plume height through application of plume model inversions **(Carey and Sparks 1986; Bonadonna and Costa 2013)**. By splitting the fall deposit into multiple layers, this technique can yield variations of mass eruption rate with time **(Sulpizio et al. 2010; Houghton et al. 2014)**. Decompression rates for particular volcanic episodes can also be determined using individual pyroclasts. For instance, the number density of vesicles generated by ascent-driven nucleation is a function of magma decompression rate (e.g., **Klug and Cashman 1996; Mourtada-Bonnefoi and Laporte 2004;**

Massol and Koyaguchi 2005; Toramaru 2006; Cluzel et al. 2008; Shea et al. 2010; Giachetti et al. 2010; Hamada et al. 2010; Martel and Iacono-Marziano 2015; Hajimirza et al. 2019; Nishiwaki and Toramaru 2019), although several processes occur in the conduit (e.g. coalescence, heterogenous nucleation, etc.) that may complicate interpretation. Another approach is to model gradients of dissolved H_2O and (if present in detectable quantities) CO_2 preserved in crystal-hosted melt reentrants to estimate the decompression rate experienced by the crystal during ascent to the surface and prior to eruption quench **(Liu et al. 2007; Myers et al. 2016, 2018)**. Although several studies have investigated the evolution of mass eruption rate with vesicle number density (and calculated decompression rate) through a volcanic sequence, no study has directly compared decompression rates determined using melt reentrants with those using vesicle number density from the same pyroclasts.

In this study we compare and contrast all three independent methods during the opening sub-Plinian and Plinian fallout phases of the Late Bronze-Age (LBA) eruption of Santorini **(Bond and Sparks 1976; Taddeucci and Wohletz 2001; Druitt 2014)**. We integrate the results with pre-existing interpretations for how eruptive activity proceeded during these eruptive phases. A major conclusion of our work is that decompression rates recorded by the deep and shallow conduit systems are decoupled, and we propose a possible explanation in the case of the LBA eruption.

Geologic Background

The Santorini volcanic field is located on the Aegean volcanic arc, within a NE-SW trending rift zone (Fig. 1a**)**. It is the most active volcanic center in the eastern Mediterranean region, having had at least twelve Plinian eruptions over the last 360 ky, interspersed with episodes of lava emission and smaller explosive events **(Druitt et al. 1999)**. The present-day (LBA) caldera is up

to 400 m deep and is cut by a prominent NE-SW lineament called the Kameni Line, which is parallel to the rift zone (Fig. 1b). Vents of historical volcanic activity are aligned along the Kameni Line, as were epicenters of the seismic unrest of 2011-12 **(Kaviris et al. 2015)**, highlighting that it is a major line of weakness in the caldera.

The LBA eruption (also commonly called the Minoan eruption) was the most recent Plinian event at Santorini, occurring ~3600 years ago. It discharged 48-86 km^3 of magma and comminuted rock debris, and collapsed a large part of the modern-day caldera. It began with sub-Plinian precursory explosions, the plumes from which were largely dispersed to the south (phase 0) **(Heiken and McCoy 1990; Cioni et al. 2000).** The eruption then evolved through four main phases (Fig. 1c): a Plinian plume (phase 1), pyroclastic surges (phase 2), low-temperature, pyroclastic flows (phase 3), and voluminous hot, fluidized pyroclastic flows (phase 4) **(Bond and Sparks 1976; Heiken and McCoy 1984; Sparks and Wilson 1990**; **Taddeucci and Wohletz 2001; Druitt 2014)**.

The vent for phase 1 has been extrapolated to a location on the Kameni Line; the plume was dispersed to the east to south-east and grew with time, producing a reversely graded pumice fall deposit preserved up to 6 m thick (**Bond and Sparks 1976; Heiken and McCoy 1984**). The resulting fall deposit has a volume of at least 1-2 km^3 dense-rock equivalent, and has been subdivided into four layers, P1a - P1d (**Druitt 2014)**. Layer P1a is crudely stratified and records an initial, unsteady Plinian plume; layer P1b is non-stratified and records a steadier plume. Layer P1c is a thin pyroclastic surge bed (commonly referred to in previous publications as the 'phreatomagmatic break' or 'flow break'); it is overlain by layer P1d, the last fall layer prior to the transition to eruptive phase 2 (Figs. 1c, 2c,d).

In this paper we focus solely on the fall deposits of phases 0 and 1. Juvenile pyroclasts in these phases are white rhyodacite pumices, microphenocryst-rich andesitic pumices, and (in the upper portion P1b) cauliform andesitic enclaves. Although the rhyodacite pumices account for > 99% of all LBA magma erupted, microphenocryst-rich pumices can comprise 40-90% of the juvenile material in P0 and the lower levels of P1 (see Table 1 from **Druitt 2014**). The influx of cauliform andesitic enclaves occurs part way up layer P1b, with their size increasing in conjunction with those of the rhyodacitic pumices and lithic clasts. The microphenocryst-rich pumices and cauliform andesitic enclaves are inferred to represent a separate magma intrusion that was intersected during the tapping of the main rhyodacitic reservoir (**Druitt 2014**). In this study we focus on the rhyodacitic pumices, and the cauliform enclaves and microphenocryst-rich pumices are not considered. Previous work of **Wilson and Houghton (1990**) noted only a slight decrease in rhyodacitic pumice density (~0.6 to ~0.5 kg/m^3), and overall consistent vesicularity (73-82%), upwards through P1.

Lithic components in the LBA fallout units have been interpreted to record changing levels of fragmentation with time (**Druitt 2014**). Lithics in P0 and at the base of P1 are dominated by lavas, inferred to be shallowly derived. About mid-way through P1b the proportion of altered lava lithics increases, and hydrothermally iron-stained blocks of holocrystalline to glass-bearing granitoids appear in abundance (Figs. 1c, 2b). These then increase in size and abundance to the top of P1b, where they account for a third of the lithic assemblage. Following the first pyroclastic surge (P1c), the final fall layer (P1d) is again dominated by fresh lavas. Making the assumption that free lithics are derived from or above the fragmentation level (e.g. **Barberi et al. 1989)**, the data indicate that the magma fragmentation level was shallow during phase P1a, then descended with time, reaching the top of melt-bearing plutonic lithologies towards the end of phase P1b.

Phase equilibria experiments and melt inclusion volatile contents have constrained the pre-eruptive storage conditions of the ~70 wt. % SiO_2 rhyodacite to 850-880 °C, 100-160 MPa, 4-5 wt.% H_2O and <200 ppm CO_2 **(Cottrell et al. 1999; Cadoux et al. 2014; Druitt et al. 2016**; **Flaherty et al. 2018).**

Methods

We divided the fall deposit into six layers, expanding upon the original four: P0, P1a1, P1a2, P1b1, P1b2, and P1d (Figs. 1c, Fig. 2*)*. Layer P1a1 is defined by two reversely zoned units with the transition to P1a2 marked by a coarsening of grain size (Fig. 2c, d). A thin parting of coarse ash separates layers P1a2 and P1b1, indicating a transient lowering of the eruption plume. The boundary between P1b1 and P1b2 is identified by the first appearance of cauliform andesitic enclaves. The six layers could be traced between multiple sites around the caldera rim. Maximum lithic size and fall layer thickness measurements were made at 43 localities (see Supplementary Table 1) to determine the evolution of plume height, wind direction, and mass eruption rate during phases 0 and 1, following the methods of **Carey and Sparks (1986)**. For each site, layer thickness was measured at several local sections, and an average was used on the isopach map (Fig. 3). Following the recommendations of **Biass and Bonadonna (2011)**, three dimensions of the five largest lithic clasts from a 1 m^2 section were measured for each fall layer, and the mean of these five averaged diameters was used to create a lithic isopleth map (Supplementary Table 1). Thickness and lithic measurements for P0 were presented previously by **(Cioni et al. 2000)**. We use their estimate for phase 0 plume height and convert it to mass eruption rates in the same way as for our phase 1 data (see Table 1).

158 Single pumice clasts were collected from within each of the six fall layers, with three
159 samples collected from the thick P1b (lower, middle, upper), resulting in eight samples for this
160 study – one in P0 and seven in P1 (Supplementary Table 2). Given the restricted range of pumice
161 vesicularity and densities (**Wilson and Houghton 1990**), no particular clast density class was
162 targeted. All samples from P1 were analyzed for melt reentrants and vesicle number density from
163 single pumice clasts; P0 pumices are significantly smaller (< 5 cm) than those of P1 used in this
164 study (6-13 cm: Supplementary Table 2), requiring multiple clasts to be crushed to obtain enough
165 crystals to find melt reentrants. The pumices were scrubbed to remove any adhering ash matrix,
166 and to ensure that microphenocryst-rich pumices were avoided, as they may have had a different
167 decompression history. Effort was made to avoid pumices with strongly elongated vesicles
168 (**Taddeucci and Wohletz 2001**), which would affect estimation of vesicle number density. For
169 vesicle analysis, we chose to focus on the rim of each pumice clast, as rims are less likely to have
170 been affected by post-fragmentation vesicle growth and coalescence (**Thomas et al. 1994; Shea**
171 **et al. 2010**). Vesicle Number Densities from thick sections of pumice rims, were imaged using a
172 Scanning Electron Microscope at image magnifications from ×25 up to ×1000, and then quantified
173 by analyzing six ×500 and two ×1000 images per pumice clast in FOAMS (**Shea et al. 2010**). The
174 choice of analyzing these two high magnifications serves to focus our counting on the smallest
175 vesicles, which dominate vesicle number density (**Houghton et al. 2010**). In our calculations we
176 assumed a constant vesicularity of 75%, based upon the relatively homogenous vesicularity data
177 of **Wilson and Houghton (1990**). Full processing procedures and discussion of error analyses can
178 be found in the Supplementary Material.
179 The remaining portions of each pumice clast were crushed using a mortar and pestle, sieved
180 to 250- and 500-μm size fractions, and picked for plagioclase, clinopyroxene and orthopyroxene.

All selected crystals were coated in vesiculated glass (Supplementary Figure 1). The crystal separates were then submerged in isopropyl alcohol to search for melt reentrants. This method worked well for plagioclase, but for the darker pyroxenes it was commonly necessary to mount the crystals in Crystalbond, slightly polish into their interiors, and use an optical microscope to search for melt reentrants. Plagioclase was found to contain the majority of melt reentrants (perhaps due to the challenge of observing them in the pyroxenes), mostly situated on crystal faces. Due to the requirements of the 1D diffusion code (see below for more information), care was taken to select only those rare melt reentrants with a simple morphology (i.e. no bottle neck, internal vesicles or minerals, multiple tubes, etc.), which would complicate diffusion assumptions (Supplementary Figure 2). We also selected reentrants with a single vesicle at their mouths to ensure efficient diffusive exchange between the reentrant and the degassing, external melt (after **Lloyd et al. 2014)**. Using this criterion, only a few melt reentrants were found per 50-100 crystals, although this was quite variable between layers. Sixteen melt reentrants in total were studied (Fig. 4): fourteen in plagioclase, one in orthopyroxene and one in clinopyroxene. All melt reentrants were measured along their lengths (ranging from 80 to 320 μm) for H_2O and CO_2 concentrations using a Thermo-Nicolet Nexus 670 Fourier transform infrared spectrometer (FTIR) interfaced with a Continuum IR microscope at the University of Oregon using a computer-controlled stage. Of these sixteen melt reentrants, five were found to have flat profiles and were not able to be fit using the diffusion model; these reentrants were not further evaluated. Following FTIR analysis at the University of Oregon (FTIR-UO), eight of the eleven melt reentrants were re-analyzed (3 were lost in this process) at the University Clermont Auvergne by FTIR (FTIR-UCA) and Raman spectroscopy (Raman-UCA). This allowed us to evaluate the dependence of modeled

decompression rates on the measured profiles. All methods for these three separate instruments, and detailed transect information, can be found in the Supplementary Material.

To model the measured H_2O diffusion profiles, we applied the 1-D constant decompression model of **Myers et al. (2018).** This model, based on that of **Liu et al. (2007)**, allows for comparison of the measured and simulated profiles for various decompression rates. The boundary condition at the contact between the host melt and the mouth of the melt reentrant is based on the melt H_2O and CO_2 solubility at a given pressure, updated at each decompression step, and is assumed to be in equilibrium with the external melt outside the crystal (**Liu et al. 2007; Myers et al. 2016, 2018**).

Results

Plume heights and mass eruption rates

Isopach and lithic isopleth maps for phase P1 are shown on Fig. 3. The broadening of isopleths upwards in the fall deposit (Fig. 3b-f) records an increase in plume height with time (particularly between P1b1 and P1b2), prior to a decrease in P1d. Wind direction recorded by the isopleths changes from SSE-wards in P1a1 and P1a2, to E-wards in P1b1, to NE-wards in P1b2. Layer P1d appears to have little wind influence on its dispersion. Wind directions recorded by isopach maps of the same levels agree with those for the isopleths for P1a, but disagree for P1b, where isopach wind directions are less rotated than those indicated by the isopleths (Fig. 3a vs. g). This could be due to the fact that each fallout layer is integrating an overall increase in eruption intensity throughout its thickness, so that the upper portion of the layer is probably where the largest clasts reside. Essentially, where the isopleths are recording the wind direction of the upper portion of any given layer, the isopach thickness is averaging the wind direction of that entire layer.

225 Plume heights for each layer are estimated using the **Carey and Sparks (1986)** inversion
226 model (Table 1 and Fig. 5). As the height estimate is based solely on the crosswind range (half
227 width of the depositional envelope), uncertainties presented for plume height are based on the
228 'wiggle-room' available in the crosswind range isopleth placement (Fig. 3*)*. Conversion of isopleth
229 data to plume height used the 3.2 cm contour, the only one available for all five layers, although
230 this is loosely constrained for P1a1 and P1a2 (Fig. 3). Plume height estimates were also made for
231 the few other isopleths available, however agreement is typically poor between conversions
232 (Supplementary Figures 3 and 4). Although it is feasible to take an average plume height based on
233 several isopleths, because this can only be completed for certain layers, with quality of isopleths
234 not all being equal, we have chosen to focus our interpretations on the 3.2 cm isopleth. Taking 8.5
235 ± 1.5 km as the estimated plume height for P0 (**Cioni et al. 2000**), the 3.2 cm isopleths suggest an
236 initial increase in plume height, with the greatest height of 28.4 ± 1.0 km reached in P1b2,
237 decreasing to 21.7 ± 1.1 km in P1d, following initial pyroclastic surge (P1c) production (Fig. 5*,*
238 Supplemental Figure 4).
239 Plume heights were converted to mass eruption rate using the methods of **Wilson and**
240 **Walker (1987)** and **Mastin et al. (2009),** yielding values of 1.7×10^6 to 2.1×10^8 kg s^{-1} and $1.0 \times$
241 10^6 to 1.5×10^8 kg s^{-1}, respectively (Table 1). Error bars associated with the Wilson and Walker
242 (1987) estimates are propagated based on those determined for each plume height (Table 1).
243 Although the conversion based on the **Wilson and Walker (1987)** formula is consistently higher,
244 it falls within error of the **Mastin et al. (2009)** value (Table 1). Importantly, the relative range of
245 two orders of magnitude represented by P0 and P1 is consistent between the two methods. The
246 lowest mass eruption rate is associated with P0, and the highest with P1b2 (Fig. 5).
247

Decompression rates from pumice Vesicle Number Densities

Visually there is a noticeable change in the sizes of vesicles in the rims of pumice clasts up through P0 and P1, with smaller (average diameter 4-5 μm) vesicles found at the top of P1a and the top of P1b (Fig. 6, Table 2). The largest vesicles, with average diameters of 9-13 μm, are observed in P0 (largest), at the base of P1a, at the base of P1b, and in P1d. Pumice-rim vesicle number density values span 1.5 orders of magnitude, from 2.50×10^6 to 6.56×10^7 mm^{-3}, falling within the range typical for explosive rhyolitic eruptions (**Giachetti et al. 2010; Houghton et al. 2010**). The lowest vesicle number density is from P0, and the highest is from P1b2.

Vesicle number densities were converted to decompression rates using equation (2) from **Toramaru (2006)**. This requires estimates of the interfacial tension between H_2O and melt, the starting saturation pressure and temperature, and the melt H_2O diffusivity, where the largest uncertainty comes from the choice of interfacial tension **(Shea 2017)**. Using a temperature (850 °C), pressure (165 MPa) and H_2O content (5.2 wt.%) appropriate for the LBA magma (**Druitt et al. 2016; Flaherty et al. 2018**), the diffusivity of H_2O is found to be 1.1×10^{-11} m^2 s^{-1} (equation 27 from **Zhang et al. 2007)**. The only remaining unknown is the interfacial tension, which relies on whether vesicle nucleation was homogenous or heterogeneous. We estimate decompression rates using both nucleation mechanisms, where the interfacial tension is taken to be 0.025 N m^{-1} and 0.12 N m^{-1} for heterogeneous and homogeneous nucleation, respectively **(Shea 2017**). Resulting decompression rates recorded by the vesicle number densities are 2-19 MPa s^{-1} (heterogeneous) or 50-450 MPa s^{-1} (homogeneous). In each case, the lowest rate is from P0 and the highest is from P1b2 (Fig. 5).

Melt Reentrant Volatile Profiles

Of a total of eleven measured H_2O profiles in melt reentrants, nine display gradual decreases in H_2O concentration as the transect approaches the crystal rim and the remaining two preserve slightly flatter profiles (Supplementary Figure 5). Some variabilities in H_2O concentrations and gradients are observed between the three instruments used (FTIR-UO, FTIR-UCA, Raman-UCA), but the shape of each diffusion profile is usually similar (Fig. 7, Supplementary Table 4). Most melt reentrants measured by FTIR spectroscopy contain interior H_2O concentrations (H_2O = 2.0-5.0 wt.%) lower than those found in isolated melt inclusions in the same phenocryst phases (H_2O = 4.0-5.4 wt.%, Table 2 of **Druitt et al. 2016**); however, some H_2O concentrations determined by Raman spectroscopy (H_2O = 3.2-5.9 wt.%) are higher than those found by FTIR. The absence of detectable CO_2 in the melt reentrants is not surprising given the low concentrations of CO_2 in isolated melt inclusions (<200 ppm; **Druitt et al. 2016**) and compared to other silicic systems (**Myers et al. 2018**).

All 1-D decompression models requires an estimate of the starting pressure, initial dissolved H_2O concentration, temperature, and exsolved gas content. Models were run assuming a pre-eruptive temperature of 850 °C, a constant decompression rate and isothermal conditions. A starting pressure (165 MPa) and H_2O concentration (5.2 wt.%) were determined based on the lack of measurable CO_2, but relatively high H_2O, measured in the interiors of most melt reentrants. This pressure is broadly consistent with that estimated from melt inclusions (100-160 MPa**)**, with H_2O concentrations representing upper end values measured from melt inclusions, but with CO_2 at the lower end of the dataset (**Druitt et al. 2016)**. To objectively choose the best-fit profile, we used an iterative grid-search function to optimize fitting of the measured profiles (**Myers et al. 2018)**. Unlike in **Myers et al. (2018),** we cycled through a range of decompression rates and fragmentation pressures (pressure where diffusion ceases in the model), rather than initial gas

294 content. This allowed us to test whether the selected best-fit fragmentation pressure shifts with
295 time during eruption. For low-CO_2 systems, the selected decompression rate is less sensitive to
296 starting gas content, so we assumed no initial exsolved gas phase.

297 It was found that for those melt reentrants where concentration profiles were measured by
298 all three methods (eight of eleven), modeled decompression rates were fairly consistent (Fig. 5;
299 Supplementary Figure 5). Good model fits for all profiles could be achieved using our pre-ascent
300 storage pressure estimate of 165 MPa. Hereon, we focus on the decompression results based on
301 the University of Oregon FTIR, where all eleven melt reentrants were measured. The resulting
302 decompression rates range between 0.008 and 0.25 MPa s^{-1}, but without any systematic variation
303 with stratigraphic height (Fig. 5). For those layers where multiple melt reentrants were measured
304 and modeled (RDP18, RDP13 and RDP5) agreement between the different decompression rate
305 estimates is good, especially compared to the two orders of magnitude represented by the entire
306 dataset (Fig. 5).

307

308 **Discussion**

309 *Time variations in plume height and mass eruption rate*

310 Our isopleth data indicate that the plume rose from P0 to P1b, before diminishing in height
311 after production of the pyroclastic surges of P1c (Fig. 5). Previous estimates placed the maximum
312 plume height for phase 1 at 36 ± 5 km, with a maximum eruption rate of 1.4 - 4.2 × 10^8 kg s^{-1}
313 (**Sigurdsson et al. 1990, Sparks and Wilson 1990**, based on the data of **Bond and Sparks 1976)**.
314 Our estimate of maximum plume height is lower than this (layer P1b2: plume height 28.4 ± 1.0
315 km, mass eruption rate 2.1 ± 0.6 × 10^8 kg s^{-1} based on **Wilson and Walker 1987**), probably because

316 we restricted sampling to a 1 m^2 area, whereas **Bond and Sparks (1976)** sampled over the entire
317 outcrop (R.S.J. Sparks, written communication).
318
319 *Comparison of the decompression rate estimates*
320 Calculated magma decompression rates based on vesicle number density differ by more
321 than an order of magnitude, depending on the nucleation assumption (2-19 MPa s^{-1} - heterogeneous
322 or 50-450 MPa s^{-1} - homogeneous; Fig. 5). Homogenous nucleation is commonly assumed to
323 dominate in more evolved melts (**Mangan and Sisson 2000)** since silicate minerals are thought to
324 be poor nucleation sites for vesicles **(Hurwitz and Navon 1994)**. Much of the requirement for
325 heterogenous nucleation is based on the presence of Fe-Ti oxides, long established as the best
326 nucleation site for vesicles (**Hurwitz and Navon 1994**). However, a review of vesicle size
327 distributions and magma decompression rates by **Shea (2017)** demonstrates that the assumption of
328 homogenous nucleation, and the resulting interfacial tension value, produces decompression
329 estimates that are inconsistent with other nucleation-based rate-meters, and often requires
330 overpressures greater than the inferred depth of storage. **Shea (2017)** argues that heterogenous
331 nucleation is likely in all magmas (basaltic through rhyolitic), perhaps facilitated by oxide
332 nanolites. The following lines of evidence suggest that heterogenous nucleation occurred during
333 ascent of the LBA magma: (1) H_2O gradients measured in reentrants can be modeled by constant
334 decompression from the storage region to the fragmentation level, requiring that diffusion to a
335 degassing external melt was occurring early on in magma ascent (and hence that the external melt
336 was growing vesicles); (2) apparent nucleation of vesicles on Fe-Ti oxide grains contained within
337 melt reentrants (Supplementary Figure 2 – not evaluated for H_2O profiles/decompression rate).

Even assuming heterogeneous nucleation, the decompression rates from melt reentrants (0.008 to 0.25 MPa s^{-1}, average 0.06 MPa s^{-1}) are 2-3 orders of magnitude lower than those based on vesicle number density (2-19 MPa s^{-1}), although they each span about an order of magnitude. Previous workers have also noted discrepancies between the rates retrieved from melt reentrants and those from vesicles (**Shea 2017; Cassidy et al. 2018)**. The offset can be understood by considering the kinetics of the two processes. While vesicles nucleate on timescales of seconds in response to rapid magma decompression (e.g., **Toramaru 2006; Hajimirza et al. 2019; Nishiwaki and Toramaru 2019**), the ability of a H_2O gradient in a melt reentrant to react to external decompression is limited by the rate of H_2O diffusion in melt. Melt reentrants will cease recording diffusive H_2O loss if the magma decompression rate becomes too fast. **Liu et al. (2007)** estimate this threshold to be ~0.25 MPa s^{-1} in silicic systems, which indeed corresponds to the uppermost decompression rates reported here and by **Myers et al. (2018)**. While melt reentrants are unable to record decompression rates much higher than this value, vesicle number densities can record much faster rates (**Shea 2017**). The offset in decompression rates estimated by the two methods suggests that the decompression rate of the magma increased during ascent, from <0.25 (recorded by melt reentrants) to >>0.25 MPa s^{-1} (recorded by vesicles). We envisage two possible explanations, distinguishing between deeper and shallower levels of the feeder conduit.

1. *Nonlinear pressure gradient during ascent to the fragmentation level.* As the magma ascends the feeder conduit, water diffuses from the melt to vesicles and the magma vesiculates. The mixture of gas and melt is then accelerated to the surface and undergoes fragmentation. During this process the magma can experience rapidly accelerating decompression due to: (1) increasing gas fraction as the magma degasses and the gas phase

expands (i.e., mass continuity); (2) large (>> lithostatic) nonlinear pressure gradients immediately beneath the fragmentation level due to the marked increase in melt viscosity as the dissolved water content decreases **(Cashman and Scheu 2015; Gonnerman, 2015)** (as a silicic melt with 5 wt.% water degasses to 1 wt.% water, its viscosity increases by 2-3 orders of magnitude **(Giordano et al. 2008; Romine and Whittington 2015)**; (3) rapid decompression associated with magma fragmentation. The high rates of magma decompression preceding, and accompanying, fragmentation may in some cases trigger a second vesicle nucleation event (**Massol and Koyaguchi 2005; Toramaru 2006; Hamada et al. 2010; Hajimirza et al. 2019)**.

2. *Upwardly converging magma flow*. Accelerating magma flow may also result from changes in conduit geometry with depth beneath the volcano, for example a feeder dike at depth focusing upwards into a narrow, shallow conduit. Syn-eruptive magma flow through a deep, dike-shaped conduit transitioning into a shallow cylindrical conduit has been called upon at a number of volcanoes, such as Montserrat in the Antilles **(Costa et al. 2007)** and Somma–Vesuvius in Italy **(Massaro et al. 2018).** The location of the vents of LBA phases P0 and P1 on the NE-SW-trending Kameni Line (Fig. 1b**)**, a long-lived line of weakness in Santorini caldera, suggests that it is possible that the LBA magma left its upper crustal reservoir in a dike, then converged into a more cylindrical conduit at shallow levels. This is also inferred to have occurred during historical activity at Santorini **(Pyle and Elliott 2006,** Fig. 8**).** The upward focusing of magma flow from a 2 km-long dike (the deep conduit) into a 20 m-long segment of that dike (the shallow conduit) could have increased the ascent rate of the LBA magma by two orders of magnitude, providing another possible

384 explanation of the offset between melt reentrants and vesicle number density. In this
385 mechanism, the LBA melt reentrants would record the initial slow stage of magma ascent
386 through the deeper feeder dike, and vesicle number density the much faster stage of focused
387 magma flow through the shallow conduit.
388
389 In summary, we infer that the 2-3 orders of difference between the decompression rates
390 recorded by melt reentrants and vesicles can be attributed to the non-linear pressure gradient
391 associated with the fragmentation level, possibly coupled with a downward flaring of the feeder
392 conduit. Since melt reentrants only record slower decompression conditions (<0.25 MPa s^{-1}), they
393 likely record flow during deeper magma ascent, whereas vesicle number densities are weighted
394 towards the rapid, nonlinear decompression of faster, shallow ascent associated with fragmentation
395 (Fig. 8*;* **Massol and Koyaguchi 2005; Toramaru 2006; Hamada et al. 2010; Hajimirza et al.**
396 **2019**).
397
398 *Integration of the different parameter sets*
399 We now compare time variations of the different eruption intensity proxies (Fig. 5). Mass
400 eruption rate is lowest in P0 and rises steadily to a maximum near the top of P1b, before decreasing
401 in P1d. Decompression rate from vesicle number density mimics mass eruption rate by increasing
402 from P0 to P1a2, being highest at the top of P1b2, then decreasing in P1d. However, it differs from
403 mass eruption rate in that it shows a small drop from P1a2 to P1b1. Finally, decompression rate
404 from melt reentrants increases from P0 to P1a1, then decreases markedly into P1a2 and P1b1
405 before rising again. Time-variations of the three parameters suggests: (1) magma decompression
406 rate in the deep conduit (recorded by melt reentrants) is decoupled from mass eruption rate at the

surface; (2) vesicles record rates intermediate between that in the deep conduit and the mass eruption rate; and (3) changes in decompression rate in the shallow conduit appear to lag behind those in the deep conduit (for example, the drop in decompression rate from P1a1 to P1a2 in the deep conduit occurs in vesicle number density from P1a2 to P1b1; Fig. 5).

The observed decoupling between the deep and shallow levels of the conduit may be understood if the deep conduit was a dike, as discussed earlier (Fig. 8). In eruptions fed by dikes that transition into shallow cylindrical conduits, significant decoupling of the two levels of the feeder system are possible (**Costa et al. 2007; Massaro et al. 2018**). The dike can act as a magmatic capacitor, storing magma (and pressure) by elastic deformation of the dike walls before conveying it to the fragmentation level in the shallow cylindrical conduit. The shallow conduit, generated by vent erosion, in turn modulates the mass eruption rate. Abrupt changes in deep conduit conditions can cause transient flow states, which, due to the high viscosities of silicic melts, can take several hours to propagate up into the shallow conduit (**de' Michieli Vitturi et al. 2010**). Such effects may explain why time-variations in our shallow (vesicle number density-derived) decompression rate appear to be intermediate between the deep (melt reentrant-derived) decompression rate and the mass eruption rate.

It is unclear what could have caused magma ascent rate in the feeder dike to drop by over an order of magnitude during P1a1 and P1b1. Assuming that the data are representative of the magma as a whole, one possibility is that the melt reentrants are recording short-term fluctuations in deep magma decompression rate not captured by the mass eruption rate data. While mass eruption data are layer-averaged, melt reentrants are derived from individual magma parcels (pyroclasts) and may record processes taking place on shorter timescales. The bedded nature of P1a shows that eruptive conditions early on in phase 1 were unsteady, and that quasi-steady

conditions were not attained until P1b. The occurrence of a coarse-ash parting at the P1a-P1b boundary (Figs. 1c, 2c,d) suggests that the mass eruption rate declined greatly at this point in the eruption, as supported by the decrease in decompression rate preserved by melt reentrants and VND, although not shown by our isopleth data. This suggests that melt reentrants and vesicles, due to their ability to respond rapidly to changing decompression conditions (although on subtly different timeframes), may record changes in eruption history that might not be recognized as significant time breaks in the field. The low decompression rates recorded by melt reentrants in P1a2 and at the base of P1b may therefore be inherited from early unsteadiness in deep magma flow as the conduit geometry evolved in response to changes in magma pressure and crustal stresses. Early transient flow and eruption unsteadiness might have been due to widening and lengthening of the deep feeder dyke as the eruption gained pace, as also invoked for the Pomici di Avellino eruption of Vesuvius (**Massaro et al. 2018**).

Behavior of the fragmentation level

Magma fragmentation rate is controlled by a number of factors, including magma composition, volatile content, rheology, decompression rate, and strain rate (**Cashman and Scheu 2015; Gonnerman, 2015, Cassidy et al. 2018** and references therein). The parameter variations in Figure 5 offer a possible explanation for the fall in fragmentation level during P1b, as was inferred from lithic data **(Druitt 2014**). This idea is supported by high mouth pressures preserved by melt reentrants at the P1b2 level (80-90 MPa; Supplementary Figure 6). Vertical migration of the fragmentation level will depend on the competition between the fragmentation rate and the rate of supply of magma from depth. Neither magma composition, dissolved volatile content, nor rheology changed significantly during the eruption (**Flaherty et al. 2018**). Thus, the main process

causing the fragmentation level to fall throughout P1b was likely the increasing magma flow rate in the shallow conduit. This could have increased the fragmentation rate by increasing the rates of strain, decompression and development of gas overpressure in vesicles (**Gonnerman 2015**). Indeed, the number of free crystals (relative to magma crystal content) increase upwards in fall unit P1b, which when coupled with analysis of particle populations, is consistent with increasing fragmentation rate during Plinian eruption prior to phase P1c (**Taddeucci and Wohletz 2001**). However, the apparent decline in magma supply from the deep feeder dyke early on during P1b (recorded by melt reentrants) may have also played a role by starving the fragmentation level of ascending magma. Once the fragmentation level had dropped significantly in P1b, access of seawater to the conduit, and/or the onset of plume instabilities, caused pyroclastic surge production (P1c). This was then followed by re-establishment of shallow fragmentation (inferred by lithics) and Plinian phase P1d.

Rapid Exploitation of a Pre-existing Conduit System

Previous work on the opening phases of large rhyolitic eruptions (Huckleberry Ridge, Oruanui and Bishop caldera-forming eruptions) found that melt reentrant diffusion profiles recorded at least a two-stage decompression history: (1) an initial stage of slow decompression prior to (2) a final, faster ascent associated with the explosive eruption (**Myers et al. 2018**). This explanation was required because measured diffusion profiles in crystals from the opening phases were best recreated using starting volatile concentrations lower than the pre-eruptive magma storage concentrations recorded by isolated melt inclusions. However, as the eruptions progressed (most notably the Bishop Tuff), the modeled starting conditions started to approach the storage concentrations, probably due to a transition from an initial, sluggish ascent to a fully developed

feeder system. These observations, however, are not applicable to the LBA eruption, where all melt reentrant profiles can be reproduced using pre-eruptive storage depth as the initial condition, even in phase 0 (albeit assuming low CO_2). This could suggest that either feeder development was relatively rapid in the LBA system, or that the ascending magma exploited a pre-existing zone of weakness.

Relevant to this idea is that alongside the eruption of the main rhyodacitic LBA magma, phases 0 and 1 were accompanied by a chemically and mineralogically distinct magma (preserved as microphenocryst-rich pumices) that has been interpreted previously to represent an intrusion already present beneath the Plinian vent prior to the LBA eruption (see **Druitt 2014** for full data and interpretations); indeed this other magma accounts for up to 40 % of pumice discharged during phase 0. It is therefore likely that the LBA magma exploited an already existing intrusion to reach the surface, pushing out some of its contents. Furthermore, seismic tomography has imaged a vertical cylinder of low-density rock beneath Santorini caldera extended down to 3 km, which may also suggest the existence of a long-lived structural pathway that could have been exploited by the ascending LBA magma **(Hooft et al. 2019).**

Conclusions

We have compared and contrasted three eruption intensity proxies for the sub-Plinian and Plinian opening phases of the Late Bronze-Age eruption of Santorini: plume height and mass eruption rate from lithic isopleths, magma decompression rate from pumice vesicle number densities, and magma decompression rate from H_2O diffusion gradients in crystal-hosted melt reentrants. The two decompression-rates determinations were carried out on the same suite of pyroclasts. The aim

498 was to obtain insight into what each technique records and detail the processes of conduit magma
499 flow early on in a caldera-forming eruption. The main conclusions are as follows.

500 1. Plume heights during fallout accumulation increased from 8.5 ± 1.5 km to 28.4 ± 1 km,
501 then decreased to 21.7 ± 1.1 km following a transient phase of pyroclastic surge
502 emplacement. Mass eruption rate during the fallout phases is estimated to have reached
503 210×10^6 kg s^{-1}.

504 2. Decompression rates estimated from vesicle number densities are 2-3 orders of magnitude
505 higher than those from melt reentrant H_2O diffusion gradients (0.008 to 0.25 MPa s^{-1}) if
506 heterogeneous vesicle nucleation is assumed (2-19 MPa s^{-1}), and 4 orders of magnitude
507 higher if homogeneous nucleation is assumed (50-450 MPa s^{-1}). Whereas melt reentrants
508 record slow (<0.25 MPa s^{-1}) magma decompression during flow deep in the conduit, vesicle
509 number densities record much higher rates of decompression in the shallow conduit,
510 probably due to the steep, non-linear pressure gradients associated with magma
511 fragmentation. Convergent flow from a dike-shaped deep conduit to a more cylindrical
512 shallow conduit may also in part explain the high rates of magma decompression recorded
513 by vesicles. The two methods therefore provide information on syn-eruptive magma
514 decompression rates at different levels in the conduit.

515 3. The time-variation of magma decompression rate in the deep conduit (recorded by melt
516 reentrants) is decoupled from mass eruption rate at the surface, whereas that in the shallow
517 conduit (recorded by vesicles) lies in between. Changes in shallow decompression rate
518 appear to lag behind those in deep decompression rate. A decrease in decompression rate
519 preserved by melt reentrants during the transition from unsteady to steady flow may have

resulted from transient flow phenomena in a deep feeder dike, possibly caused by an event of dike widening and/or lengthening.

4. Peak eruptive conditions during the Plinian phase were preceded by a fall in the fragmentation level, perhaps due to the increasing rates of shallow magma decompression and strain causing the rate of magma fragmentation to exceed that of magma supply from deeper in the conduit.
5. Melt reentrants and vesicles, due to their ability to respond rapidly to changing decompression conditions, may record changes in eruption history that might not be recognized as significant time breaks in the field.
6. The data support a previously published interpretation that the LBA magma made its way to the surface through a pre-existing zone of weakness, likely associated with an intrusion related to an earlier phase of magma movement.

Acknowledgements

The authors would like to thank Bruce Houghton for conversations surrounding isopleth/isopach data, and helpful reviews by the editor, one anonymous reviewer and Alessandro Vona that led to an improved manuscript. This work was funded through a Clermont Auvergne University Postdoctoral grant to Druitt and an NSF grant EAR-1922513 to Myers. We thank Christophe Constantin for thin sections, Jean-Marc Hénot for assistance with the SEM, and Erica Duncan, Emma Kerins, Megan Saalfeld, and Crystal Christensen for processing SEM images. This is Laboratory of Excellence ClerVolc Contribution Number 448.

References

543 Barberi F, Cioni R, Rosi M, et al (1989) Magmatic and phreatomagmatic phases in explosive
544 eruptions of Vesuvius as deduced by grain-size and component analysis of the pyroclastic
545 deposits. J Volcanol Geotherm Res 38:287–307. https://doi.org/10.1016/0377-
546 0273(89)90044-9

547 Biass S, Bonadonna C (2011) A quantitative uncertainty assessment of eruptive parameters
548 derived from tephra deposits: the example of two large eruptions of Cotopaxi volcano,
549 Ecuador. Bull Volcanol 73:73–90. https://doi.org/10.1007/s00445-010-0404-5

550 Bonadonna C, Costa A (2013) Plume height, volume, and classification of explosive volcanic
551 eruptions based on the Weibull function. Bull Volcanol 75:742.
552 https://doi.org/10.1007/s00445-013-0742-1

553 Bond A, Sparks RSJ (1976) The Minoan eruption of Santorini, Greece. J Geol Soc 132:1–16.
554 https://doi.org/10.1144/gsjgs.132.1.0001

555 Cadoux A, Scaillet B, Druitt TH, Deloule E (2014) Magma Storage Conditions of Large Plinian
556 Eruptions of Santorini Volcano (Greece). J Petrol 55:1129–1171.
557 https://doi.org/10.1093/petrology/egu021

558 Carey S, Sparks RSJ (1986) Quantitative models of the fallout and dispersal of tephra from
559 volcanic eruption columns. Bull Volcanol 48:109–125.
560 https://doi.org/10.1007/BF01046546

561 Cashman KV, Scheu B (2015) Magmatic fragmentation. The encyclopedia of volcanoes (pp.
562 459-471). Academic Press.

563 Cassidy M, Manga M, Cashman K, Bachmann O (2018) Controls on explosive-effusive volcanic
564 eruption styles. Nat Commun 9:2839. https://doi.org/10.1038/s41467-018-05293-3

565 Castro JM, Gardner JE (2008) Did magma ascent rate control the explosive-effusive transition at
566 the Inyo volcanic chain, California. Geology 36:279. https://doi.org/10.1130/G24453A.1

567 Cioni R, Gurioli L, Sbrana A, Vougioukalakis G (2000) Precursory phenomena and destructive
568 events related to the Late Bronze Age Minoan (Thera, Greece) and AD 79 (Vesuvius,
569 Italy) Plinian eruptions; inferences from the stratigraphy in the archaeological areas. Geol
570 Soc Lond Spec Publ 171:123–141. https://doi.org/10.1144/GSL.SP.2000.171.01.11

571 Cluzel N, Laporte D, Provost A, Kannewischer I (2008) Kinetics of heterogeneous bubble
572 nucleation in rhyolitic melts: implications for the number density of bubbles in volcanic
573 conduits and for pumice textures. Contrib Mineral Petrol 156:745–763.
574 https://doi.org/10.1007/s00410-008-0313-1

575 Costa A, Melnik O, Sparks RSJ, Voight B (2007) Control of magma flow in dykes on cyclic lava
576 dome extrusion. Geophys Res Lett 34:L02303. https://doi.org/10.1029/2006GL027466

Cottrell E, Gardner JE, Rutherford MJ (1999) Petrologic and experimental evidence for the movement and heating of the pre-eruptive Minoan rhyodacite (Santorini, Greece). Contrib Mineral Petrol 135:315–331. https://doi.org/10.1007/s004100050514

de' Michieli Vitturi M, Clarke AB, Neri A, Voight B (2010) Transient effects of magma ascent dynamics along a geometrically variable dome-feeding conduit. Earth Planet Sci Lett 295:541–553. https://doi.org/10.1016/j.epsl.2010.04.029

Degruyter W, Bachmann O, Burgisser A, Manga M (2012) The effects of outgassing on the transition between effusive and explosive silicic eruptions. Earth Planet Sci Lett 349–350:161–170. https://doi.org/10.1016/j.epsl.2012.06.056

Doocy S, Daniels A, Dooling S, Gorokhovich Y. The Human Impact of Volcanoes: a Historical Review of Events 1900-2009 and Systematic Literature Review. PLOS Curr Disasters 2013 Apr 16 . Edition 1.: https://doi.org/10.1371/currents.dis.841859091a706efebf8a30f4ed7a1901.

Druitt TH (2014) New insights into the initiation and venting of the Bronze-Age eruption of Santorini (Greece), from component analysis. Bull Volcanol 76:794. https://doi.org/10.1007/s00445-014-0794-x

Druitt TH, Edwards L, Mellors RM, et al (1999) Santorini Volcano. Geol Soc Mem 19:

Druitt TH, Mercier M, Florentin L, et al (2016) Magma Storage and Extraction Associated with Plinian and Interplinian Activity at Santorini Caldera (Greece). J Petrol 57:461–494. https://doi.org/10.1093/petrology/egw015

Flaherty T, Druitt TH, Tuffen H, et al (2018) Multiple timescale constraints for high-flux magma chamber assembly prior to the Late Bronze Age eruption of Santorini (Greece). Contrib Mineral Petrol 173:75. https://doi.org/10.1007/s00410-018-1490-1

Giachetti T, Druitt TH, Burgisser A, et al (2010) Bubble nucleation, growth and coalescence during the 1997 Vulcanian explosions of Soufrière Hills Volcano, Montserrat. J Volcanol Geotherm Res 193:215–231. https://doi.org/10.1016/j.jvolgeores.2010.04.001

Giordano D, Russell JK, Dingwell DB (2008) Viscosity of magmatic liquids: A model. Earth Planet Sci Lett 271:123–134. https://doi.org/10.1016/j.epsl.2008.03.038

Gonnermann HM, Manga M (2003) Explosive volcanism may not be an inevitable consequence of magma fragmentation. Nature 426:432–435. https://doi.org/10.1038/nature02138

Hajimirza S, Gonnermann HM, Gardner JE, Giachetti T (2019) Predicting Homogeneous Bubble Nucleation in Rhyolite. J Geophys Res Solid Earth 124:2395–2416. https://doi.org/10.1029/2018JB015891

Hamada M, Laporte D, Cluzel N, et al (2010) Simulating bubble number density of rhyolitic pumices from Plinian eruptions: constraints from fast decompression experiments. Bull Volcanol 72:735–746. https://doi.org/10.1007/s00445-010-0353-z

Heiken G, McCoy F (1990). Precursory activity to the Minoan eruption, Thera, Greece. In: Hardy DA (ed.) Thera and the Aegean World III, vol 2. Thera Foundation, London, pp 13–18.

Heiken G, McCoy F, Jr (1984) Caldera development during the Minoan eruption, Thira, Cyclades, Greece. J Geophys Res 89: 8441-8462

Hildreth W, Drake R (1992) Volcfin Quizapu, Chilean Andes. Bull Volcanol 54:93–125

Hooft EEE, Heath BA, Toomey DR, et al (2019) Seismic imaging of Santorini: Subsurface constraints on caldera collapse and present-day magma recharge. Earth Planet Sci Lett 514:48–61. https://doi.org/10.1016/j.epsl.2019.02.033

Houghton BF, Carey RJ, Cashman KV, Wilson CJ, Hobden BJ, Hammer JE (2010) Diverse patterns of ascent, degassing, and eruption of rhyolite magma during the 1.8 ka Taupo eruption, New Zealand: evidence from clast vesicularity. J Volcanol Geotherm Res 195:31-47.

Houghton BF, Carey RJ, Rosenberg MD (2014) The 1800a Taupo eruption: "III wind" blows the ultraplinian type event down to Plinian. Geology 42:459–461. https://doi.org/10.1130/G35400.1

Hurwitz S, Navon O (1994) Bubble nucleation in rhyolitic melts: Experiments at high pressure, temperature, and water content. Earth Planet Sci Lett 122:267–280. https://doi.org/10.1016/0012-821X(94)90001-9

Kaviris G, Papadimitriou P, Kravvariti Ph, et al (2015) A detailed seismic anisotropy study during the 2011–2012 unrest period in the Santorini Volcanic Complex. Phys Earth Planet Inter 238:51–88. https://doi.org/10.1016/j.pepi.2014.11.002

Klug C, Cashman KV (1996) Permeability development in vesiculating magmas: implications for fragmentation. Bull Volcanol 58:87–100. https://doi.org/10.1007/s004450050128

Liu Y, Anderson AT, Wilson CJN (2007) Melt pockets in phenocrysts and decompression rates of silicic magmas before fragmentation. J Geophys Res 112:B06204. https://doi.org/10.1029/2006JB004500

Lloyd AS, Ruprecht P, Hauri EH, et al (2014) NanoSIMS results from olivine-hosted melt embayments: Magma ascent rate during explosive basaltic eruptions. J Volcanol Geotherm Res 283:1–18. https://doi.org/10.1016/j.jvolgeores.2014.06.002

Mangan M, Sisson T (2000) Delayed, disequilibrium degassing in rhyolite magma: decompression experiments and implications for explosive volcanism. Earth Planet Sci Lett 183:441–455. https://doi.org/10.1016/S0012-821X(00)00299-5

Martel C, Iacono-Marziano G (2015) Timescales of bubble coalescence, outgassing, and foam collapse in decompressed rhyolitic melts. Earth Planet Sci Lett 412:173–185. https://doi.org/10.1016/j.epsl.2014.12.010

Mason BG, Pyle DM, Oppenheimer C (2004) The size and frequency of the largest explosive eruptions on Earth. Bull Volcanol 66:735–748. https://doi.org/10.1007/s00445-004-0355-9

Massaro S, Costa A, Sulpizio R (2018) Evolution of the magma feeding system during a Plinian eruption: The case of Pomici di Avellino eruption of Somma–Vesuvius, Italy. Earth Planet Sci Lett 482:545–555. https://doi.org/10.1016/j.epsl.2017.11.030

Massol H, Koyaguchi T (2005) The effect of magma flow on nucleation of gas bubbles in a volcanic conduit. J Volcanol Geotherm Res 143:69–88. https://doi.org/10.1016/j.jvolgeores.2004.09.011

Mastin LG, Guffanti M, Servranckx R, et al (2009) A multidisciplinary effort to assign realistic source parameters to models of volcanic ash-cloud transport and dispersion during eruptions. J Volcanol Geotherm Res 186:10–21. https://doi.org/10.1016/j.jvolgeores.2009.01.008

Miller CF, Wark DA (2008) Supervolcanoes and their explosive supereruption. Elements 4:11–15. https://doi.org/10.2113/GSELEMENTS.4.1.11

Mourtada-Bonnefoi CC, Laporte D (2004) Kinetics of bubble nucleation in a rhyolitic melt: an experimental study of the effect of ascent rate. Earth Planet Sci Lett 218:521–537. https://doi.org/10.1016/S0012-821X(03)00684-8

Myers ML, Wallace PJ, Wilson CJN, et al (2016) Prolonged ascent and episodic venting of discrete magma batches at the onset of the Huckleberry Ridge supereruption, Yellowstone. Earth Planet Sci Lett 451:285–297. https://doi.org/10.1016/j.epsl.2016.07.023

Myers ML, Wallace PJ, Wilson CJN, et al (2018) Ascent rates of rhyolitic magma at the onset of three caldera-forming eruptions. Am Mineral 103:952–965. https://doi.org/10.2138/am-2018-6225

Nishiwaki M, Toramaru A (2019) Inclusion of Viscosity Into Classical Homogeneous Nucleation Theory for Water Bubbles in Silicate Melts: Reexamination of Bubble Number Density in Ascending Magmas. J Geophys Res Solid Earth 124:8250–8266. https://doi.org/10.1029/2019JB017796

Pyle DM, Elliott JR (2006) Quantitative morphology, recent evolution, and future activity of the Kameni Islands volcano, Santorini, Greece. Geosphere 2:253. https://doi.org/10.1130/GES00028.1

Romine WL, Whittington AG (2015) A simple model for the viscosity of rhyolites as a function of temperature, pressure and water content. Geochim Cosmochim Acta 170:281–300. https://doi.org/10.1016/j.gca.2015.08.009

Shea T (2017) Bubble nucleation in magmas: A dominantly heterogeneous process? J Volcanol Geotherm Res 343:155–170. https://doi.org/10.1016/j.jvolgeores.2017.06.025

686 Shea T, Houghton BF, Gurioli L, et al (2010) Textural studies of vesicles in volcanic rocks: An
687 integrated methodology. J Volcanol Geotherm Res 190:271–289.
688 https://doi.org/10.1016/j.jvolgeores.2009.12.003

689 Sigurdsson H, Carey S, Alexandri G, Vougioukalakis G, & 10 others (2006) Marine
690 investigations of Greece's Santorini volcanic field. EOS, Trans Amer Geophys Union 87:
691 337, 342

692 Sparks RSJ, Wilson CJN (1990) The Minoan deposits: a review of their characteristics and
693 interpretation In: Hardy DA (ed.) Thera and the Aegean World III, vol 2. Thera
694 Foundation, London, pp 89-99

695 Sulpizio R, Cioni R, Di Vito MA, et al (2010) The Pomici di Avellino eruption of Somma-
696 Vesuvius (3.9 ka bp). Part I: stratigraphy, compositional variability and eruptive
697 dynamics. Bull Volcanol 72:539–558. https://doi.org/10.1007/s00445-009-0339-x

698 Taddeucci J, Wohletz KH (2001) Temporal evolution of the Minoan eruption (Santorini,
699 Greece), as recorded by its Plinian fall deposit and interlayered ash ¯ow beds. J Volcanol
700 Geotherm Res 19

701 Thomas N, Jaupart C, Vergniolle S (1994) On the vesicularity of pumice. *Journal of*
702 *Geophysical Research: Solid Earth*, *99*(B8), pp.15633-15644.

703 Toramaru A (2006) BND (bubble number density) decompression rate meter for explosive
704 volcanic eruptions. J Volcanol Geotherm Res 154:303–316.
705 https://doi.org/10.1016/j.jvolgeores.2006.03.027

706 Wilson L, Walker GPL (1987) Explosive volcanic eruptions - VI. Ejecta dispersal in plinian
707 eruptions: the control of eruption conditions and atmospheric properties. Geophys J Int
708 89:657–679. https://doi.org/10.1111/j.1365-246X.1987.tb05186.x

709 Wilson, CJN, Houghton, BF (1990) Eruptive mechanisms in the Minoan eruption: evidence from
710 pumice vesicularity. Thera and the Aegean world III, *2*, 122-128.

711 Woods AW, Koyaguchi T (1994) Transitions between explosive and effusive eruptions of silicic
712 magmas. Nature 370:641–644. https://doi.org/10.1038/370641a0

713 Zhang Y, Xu Z, Zhu M, Wang H (2007) Silicate melt properties and volcanic eruptions:
714 SILICATE MELT PROPERTIES. Rev Geophys 45:.
715 https://doi.org/10.1029/2006RG000216

716

717

718 **Figure Captions**

719 **Fig. 1** Summary of geological features of Santorini and the Late Bronze Age (LBA) eruption after Flaherty

720 et al. (2018) and references therein.

721 (a) Map of Santorini and its host rift zone, showing major normal faults (circle on the hanging wall),
722 and the three main subsidence basins. The extent of submarine ignimbrite from the LBA eruption
723 mapped from seismic profiles is shown in yellow. A location map is included as inset.
724 (b) Map of Santorini caldera, showing the products of the LBA eruption (including the three main
725 ignimbrite fans from eruptive phase 4), the outline of the shallow Cape Riva caldera that existed
726 prior to the LBA eruption, the Kameni Line, and the approximate location of the Plinian vent.
727 (c) Schematic log of the products of the LBA eruption, with the distributions of the juvenile
728 components.

729 **Fig. 2** Field photos of the Plinian pumice fall deposit of phase 1 (P1) of the eruption, with a meter stick
730 represented in each photo. (a) The pumice fall deposit overlying breccias from an earlier eruption,
731 and itself overlain by the bedded tuffs of phase 2. (b) The top of P1 showing the abundance of
732 hydrothermally stained granitoid clasts at this level. (c,d) The P1 pumice fall deposit in southern
733 Santorini where layer P1b is underlain by layer P1a, with a fine ash separating the two. The thin
734 lapilli fallout of P0 lies at the bases of these outcrops. GPS locations for each site can be found in
735 Supplementary Table 1.

736 **Fig. 3** Thickness and maximum lithic size data from 43 sample locations. (a-f) isopleth data (mean diameter
737 in cm of three axes of the five largest lithic fragments in 1 m^2 of each layer); (h-l) isopach data
738 (cm). Figures (a) and (g) summarize the wind directions inferred from each technique. P0 wind
739 direction taken from Cioni et al. (2000). The implied source vent for the eruption is shown by the
740 black dot, matching that of Bonds and Sparks (1976).

741 **Fig. 4** Photomicrographs of melt reentrants exposed in plagioclase (a-c) and pyroxene (d) crystals. All melt
742 reentrants clearly display a bubble at their mouth, a requirement to ensure that efficient diffusive
743 exchange is occurring between the reentrant and surrounding melt. Simple morphologies that
744 lacked strong bottle-necks were chosen in order to validate the 1D assumption.

745 **Fig. 5** Simplified stratigraphy of the deposits from phases 0 (P0) and 1 (P1) of the eruption. Eight pumice
746 samples (names shown in boxes) were taken from six layers (labelled in bold), with the lithic

population percentages from Druitt (2014) shown as pie diagrams. Plume heights were calculated using the Carey and Sparks (1986) model from the isopleth data in Figure 3. Errors in plume height are based on uncertainties in isoline drawing. Plume heights were converted to mass eruption rate using the formula of Wilson and Walker (1987). Decompression rates (MPa s^{-1}) are presented for melt reentrants (triangles), based on modeling of diffusion gradients preserved in plagioclase and pyroxene-hosted melt reentrants, and vesicle number densities (circles). Melt reentrant profiles were measured by FTIR spectroscopy at the University of Oregon (gray triangle), and by FTIR (open triangle) and Raman (black triangle) spectroscopy at the University of Clermont Auvergne. Vesicle number densities were converted to decompression rates using the formula of Toramaru (2006), based on the assumption of either heterogenous (gray circle) or homogenous (+ circle) vesicle nucleation. Error bars for melt-reentrant-based decompression rates are based on the goodness of fit for the modeled profiles.

Fig. 6 Scanning electron microscope images, all taken at ×500, of the eight pumice samples imaged, representing six layers of the pumice fall deposits; three pumice clasts are taken from layer P1b2. The glass is shown in white, and the vesicles in black on each image. Yellow scale in bottom right corner is 100 μm.

Fig. 7 Concentration profiles for two separate melt reentrants, RDP 18 and RDP 20, both from P1a, measured for H_2O profiles using three separate instruments. Each solid curve represents the best-fit decompression profile using the 1D diffusion model presented in Myers et al. (2018). UO: University of Oregon; UCA: University of Clermont Auvergne. For RDP 20, a fluorescent background characterizes the Raman spectra acquired at the extremities of this melt reentrant, resulting in slightly higher water contents estimated by Raman spectroscopy (see supplementary material for more analytical details).

Fig. 8 Schematic showing a snapshot in time of two possible explanations why the decompression rates recorded by melt reentrants are at least 2-3 orders of magnitude lower than those recorded by

772 vesicle number densities. The figure shows two profiles through the LBA Plinian vent: (a) one
773 perpendicular to the Kameni Line (profile A-B), and (b) the other parallel to it (profile C-D). The
774 interpretation of each profile is as follows: (a) As magma ascends and degasses in the conduit, the
775 viscosity (and hence pressure gradient) rises dramatically. Melt reentrants are thought to record
776 the relatively low decompression rates (dP/dt) deep in the conduit, and vesicle number densities
777 (VND) to record the high decompression rates associated with fragmentation. (b) An additional
778 effect may have been that the eruption was fed through a dike along the Kameni Line, which then
779 focussed into a cylindrical conduit at shallow levels. Due to upwardly converging flow, the
780 decompression rates in the dike would have been slower than those in the shallow conduit.
781
782 **Tables**
783 **Table 1:** Descriptions of each of the six fallout layers and parameters calculated from lithic
784 isopleth maps.
785 **Table 2:** Vesicle size distribution parameters for each pumice clast analyzed.
786 **Table 3:** Information from individual reentrant profiles used to constrain decompression rates
787 using the 1D code described in Myers et al. (2018). All H_2O and CO_2 measurements are based on
788 results from FTIR measurements at the University of Oregon (see Supplementary Table 6 for
789 results from the other techniques). For the diffusion model, starting pressure (Pi=165 MPa) and
790 initial H_2O content (5.2 wt.%) are based on the isolated melt inclusion data of Druitt et al.
791 (2016), where final pressure (Pf) is determined through the best-fit calculation. Conversion of
792 decompression rate (dP/dt)t to ascent rate assumes a magmastatic pressure gradient, a magma
793 density of 2600 kg m^{-3} and a magma fragmentation depth at 1 km.
794

Figures 1-8

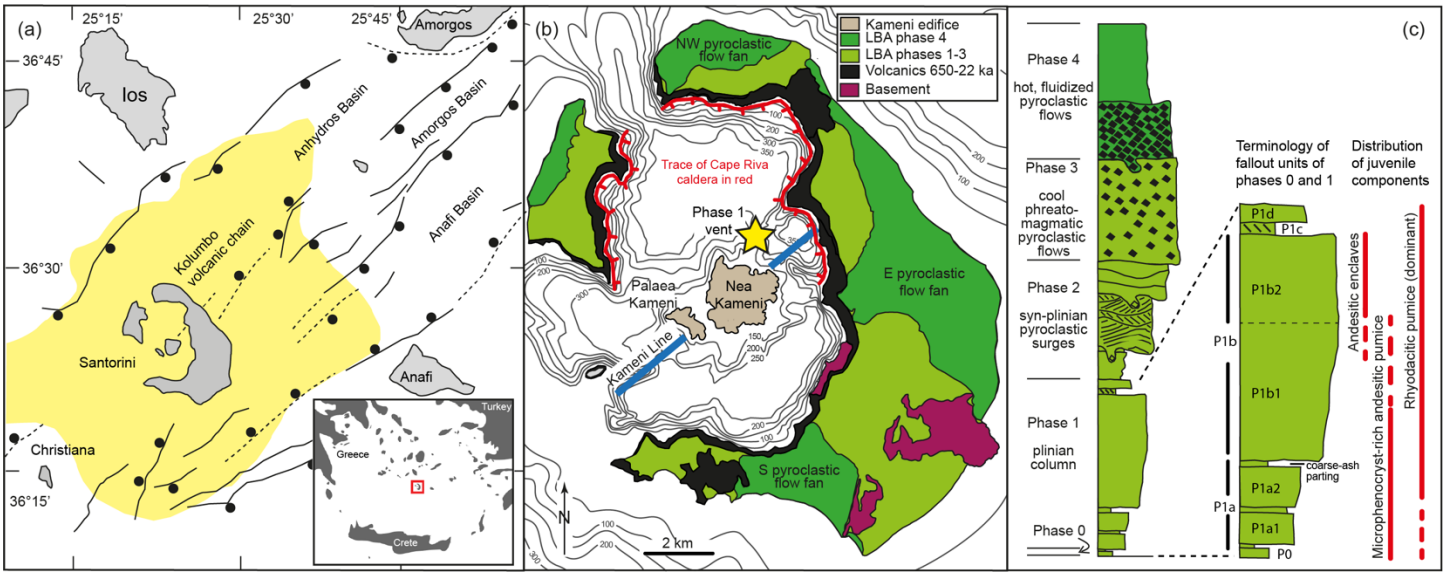

Fig. 1

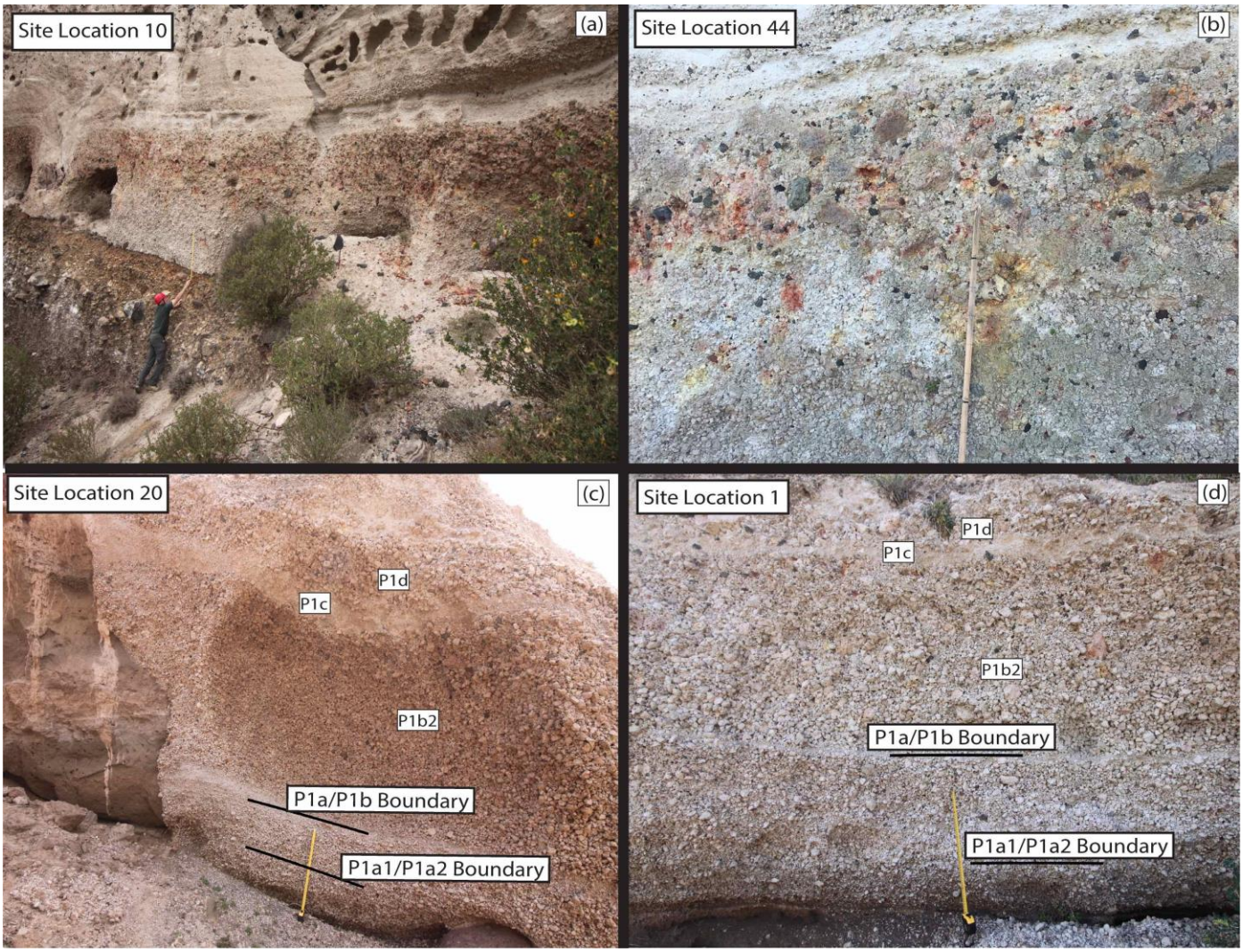
Site Location 10
(a)
Site Location 44
(b)
Site Location 20
(c)
P1d
P1c
P1b2
P1a/P1b Boundary
P1a1/P1a2 Boundary
Site Location 1
(d)
P1d
P1c
P1b2
P1a/P1b Boundary
P1a1/P1a2 Boundary

Fig. 2

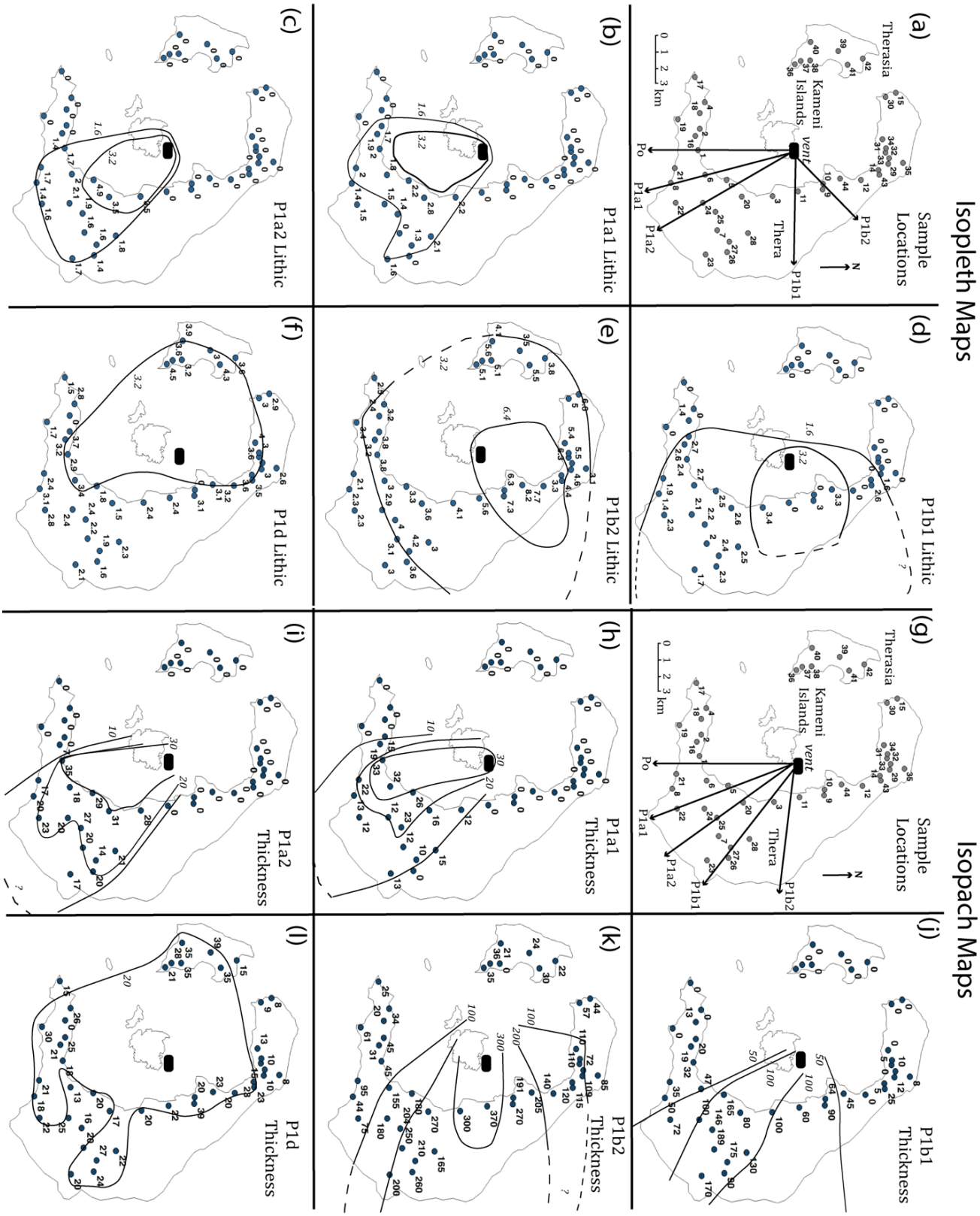
Isopleth Maps
Isopach Maps
(a)
Sample Locations
Therasia
Kameni Islands
vent
Thera
Po
P1a1
P1a2
P1b1
P1b2
0 1 2 3 km
N
(b)
P1a1 Lithic
(c)
P1a2 Lithic
(d)
P1b1 Lithic
(e)
P1b2 Lithic
(f)
P1d Lithic
(g)
Sample Locations
(h)
P1a1 Thickness
(i)
P1a2 Thickness
(j)
P1b1 Thickness
(k)
P1b2 Thickness
(l)
P1d Thickness

Fig. 3

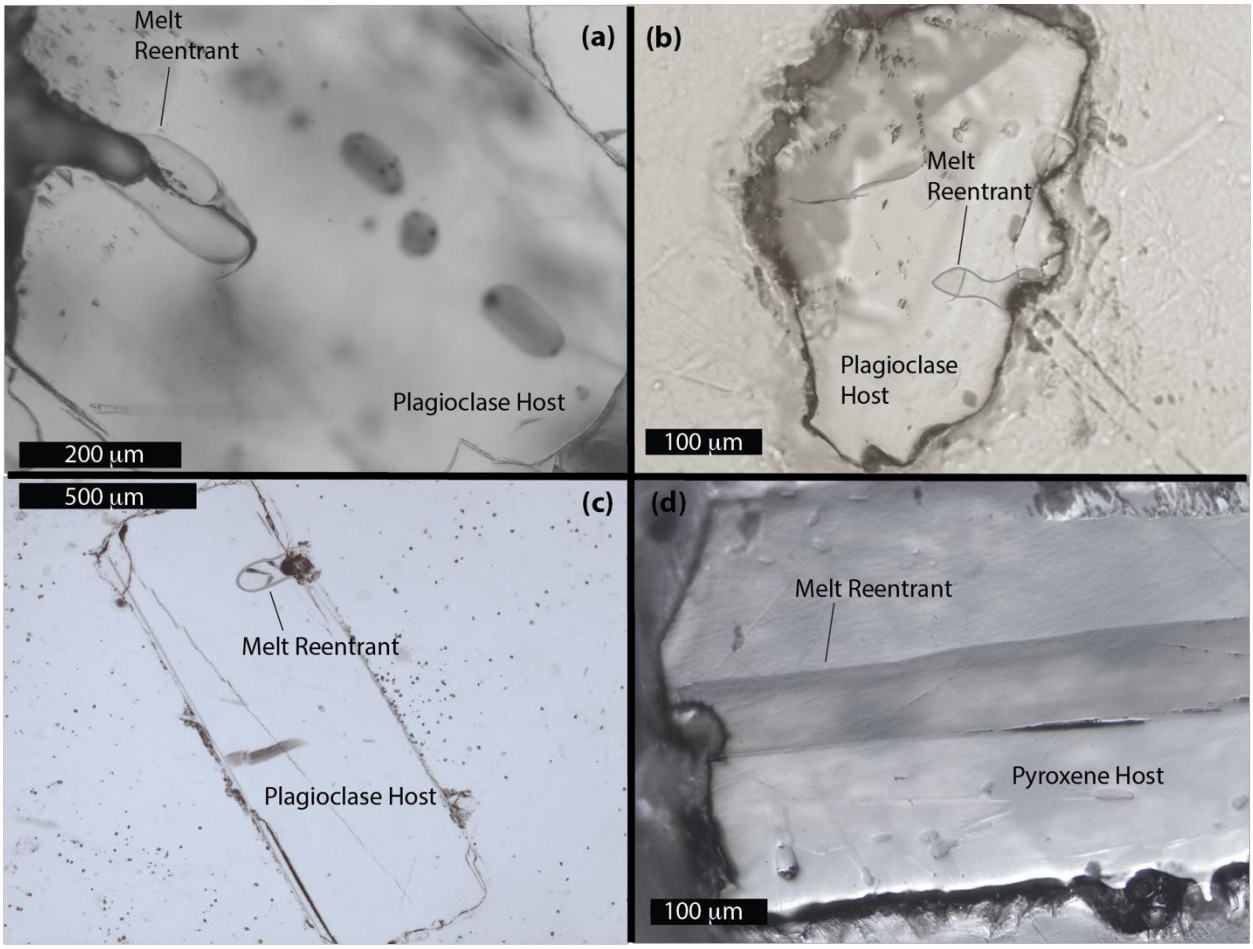
Melt
Reentrant
(a)
Plagioclase Host
200 μm
(b)
Melt
Reentrant
Plagioclase
Host
100 μm
500 μm
(c)
Melt Reentrant
Plagioclase Host
(d)
Melt Reentrant
Pyroxene Host
100 μm

Fig. 4

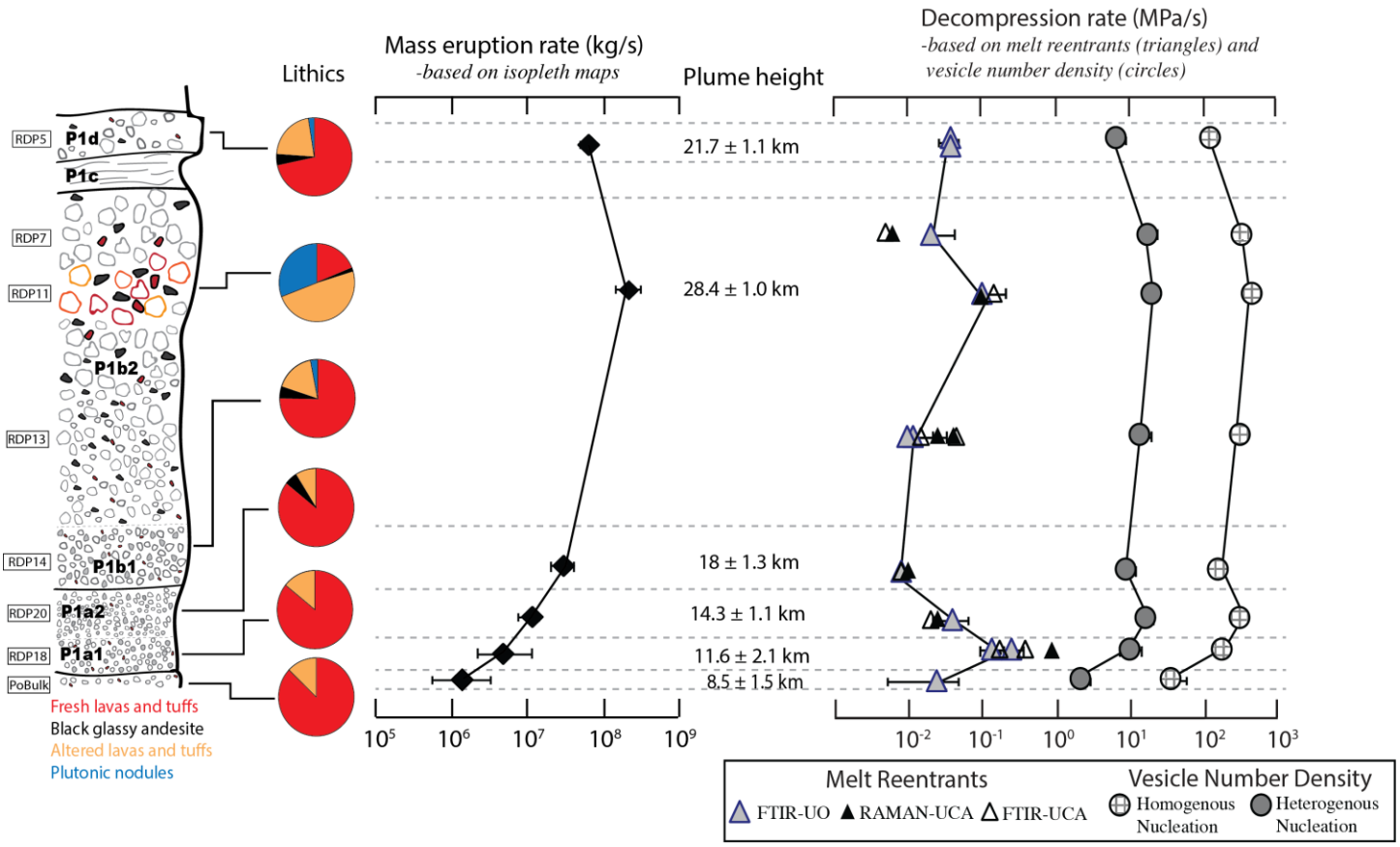
Lithics
Mass eruption rate (kg/s)
-based on isopleth maps
Plume height
Decompression rate (MPa/s)
-based on melt reentrants (triangles) and
vesicle number density (circles)
RDP5
P1d
P1c
RDP7
RDP11
P1b2
RDP13
RDP14
P1b1
RDP20
P1a2
RDP18
P1a1
PoBulk
21.7 ± 1.1 km
28.4 ± 1.0 km
18 ± 1.3 km
14.3 ± 1.1 km
11.6 ± 2.1 km
8.5 ± 1.5 km
10^5 10^6 10^7 10^8 10^9
10^-2 10^-1 10^0 10^1 10^2 10^3
Fresh lavas and tuffs
Black glassy andesite
Altered lavas and tuffs
Plutonic nodules
Melt Reentrants
FTIR-UO RAMAN-UCA FTIR-UCA
Vesicle Number Density
Homogenous Nucleation
Heterogenous Nucleation

Fig. 5

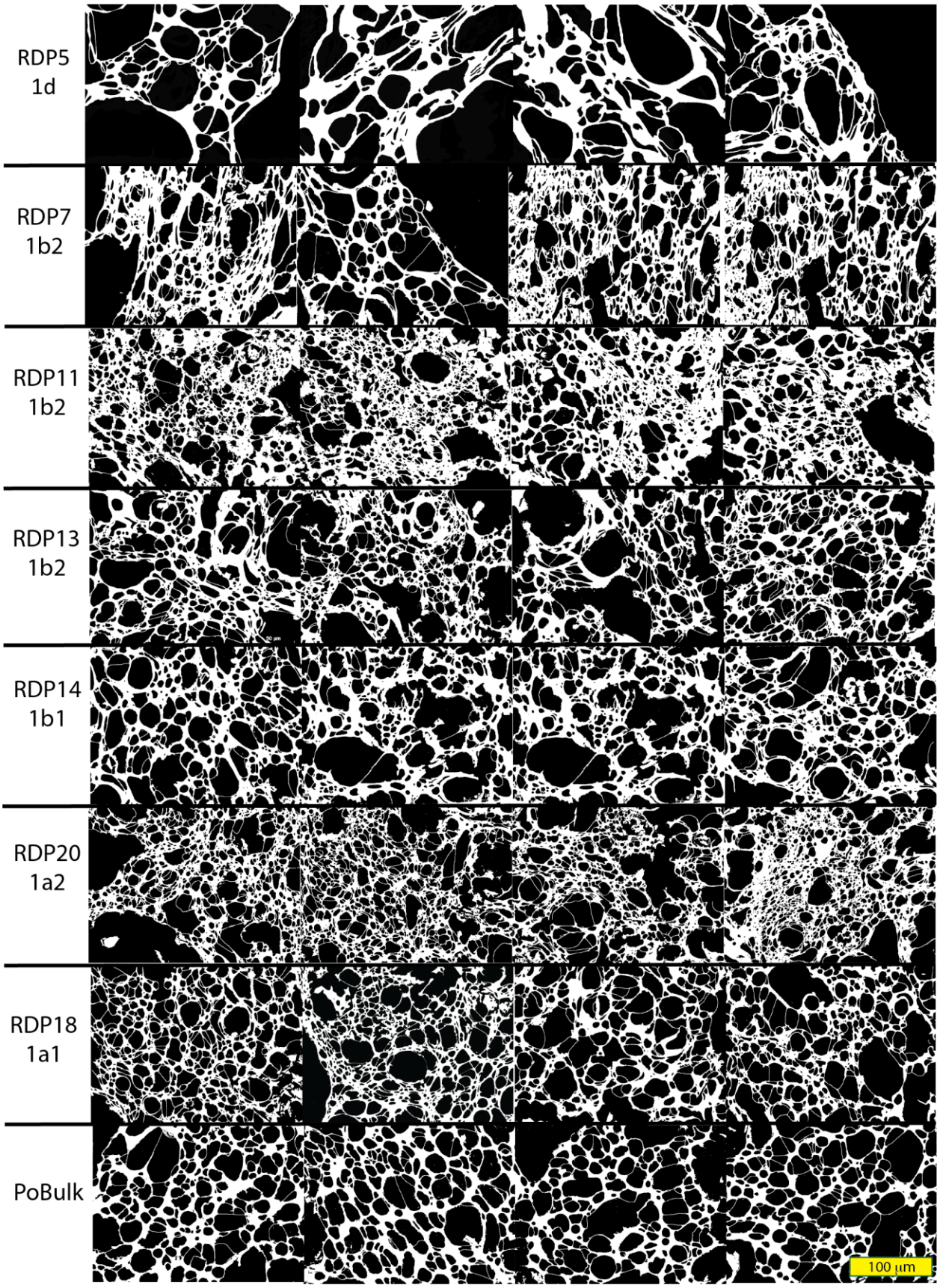
RDP5
1d
RDP7
1b2
RDP11
1b2
RDP13
1b2
RDP14
1b1
RDP20
1a2
RDP18
1a1
PoBulk
100 µm

Fig. 6

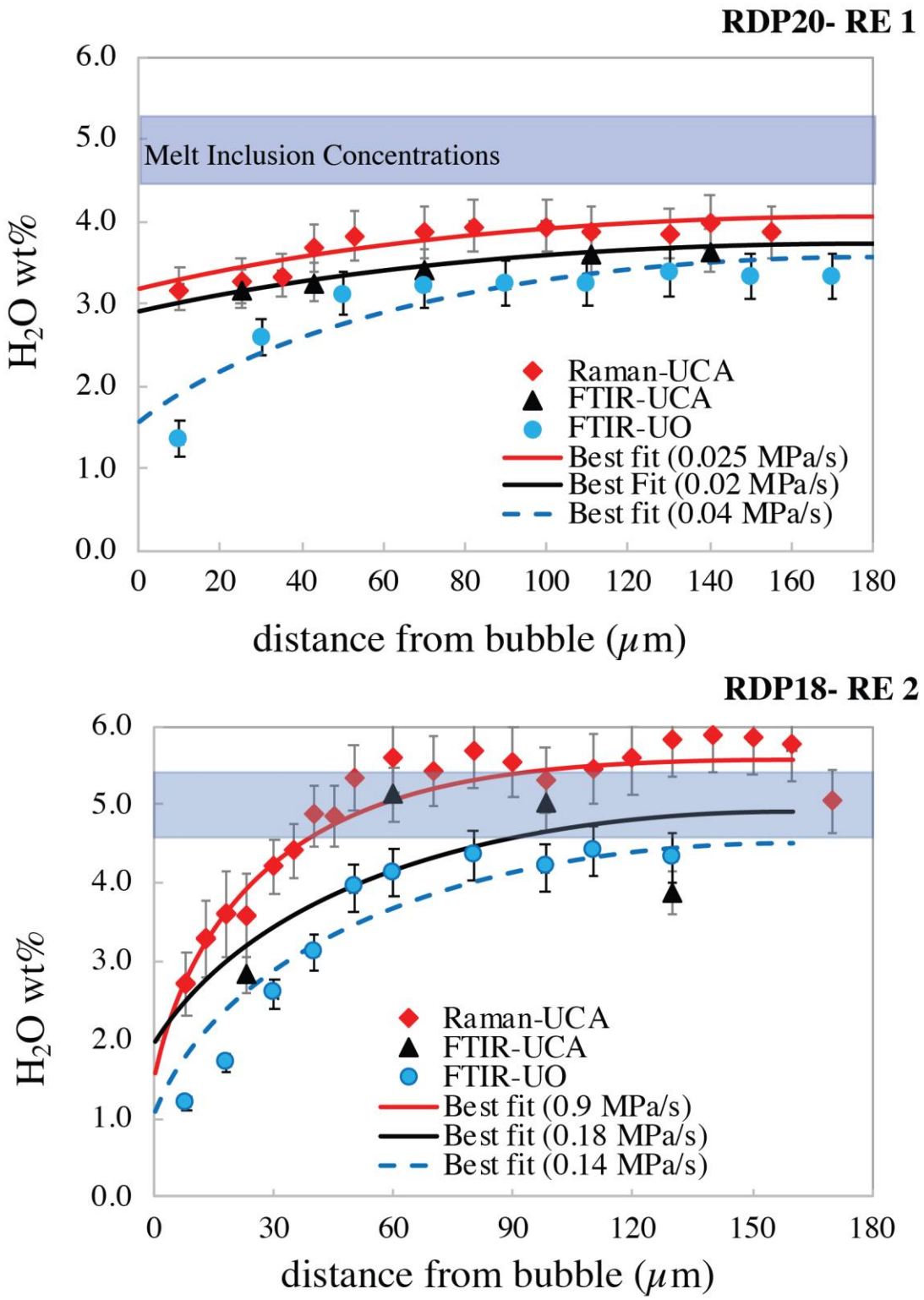
RDP20- RE 1
Melt Inclusion Concentrations
Raman-UCA
FTIR-UCA
FTIR-UO
Best fit (0.025 MPa/s)
Best Fit (0.02 MPa/s)
Best fit (0.04 MPa/s)
H2O wt%
distance from bubble (μm)
RDP18- RE 2
Raman-UCA
FTIR-UCA
FTIR-UO
Best fit (0.9 MPa/s)
Best fit (0.18 MPa/s)
Best fit (0.14 MPa/s)
H2O wt%
distance from bubble (μm)

Fig. 7

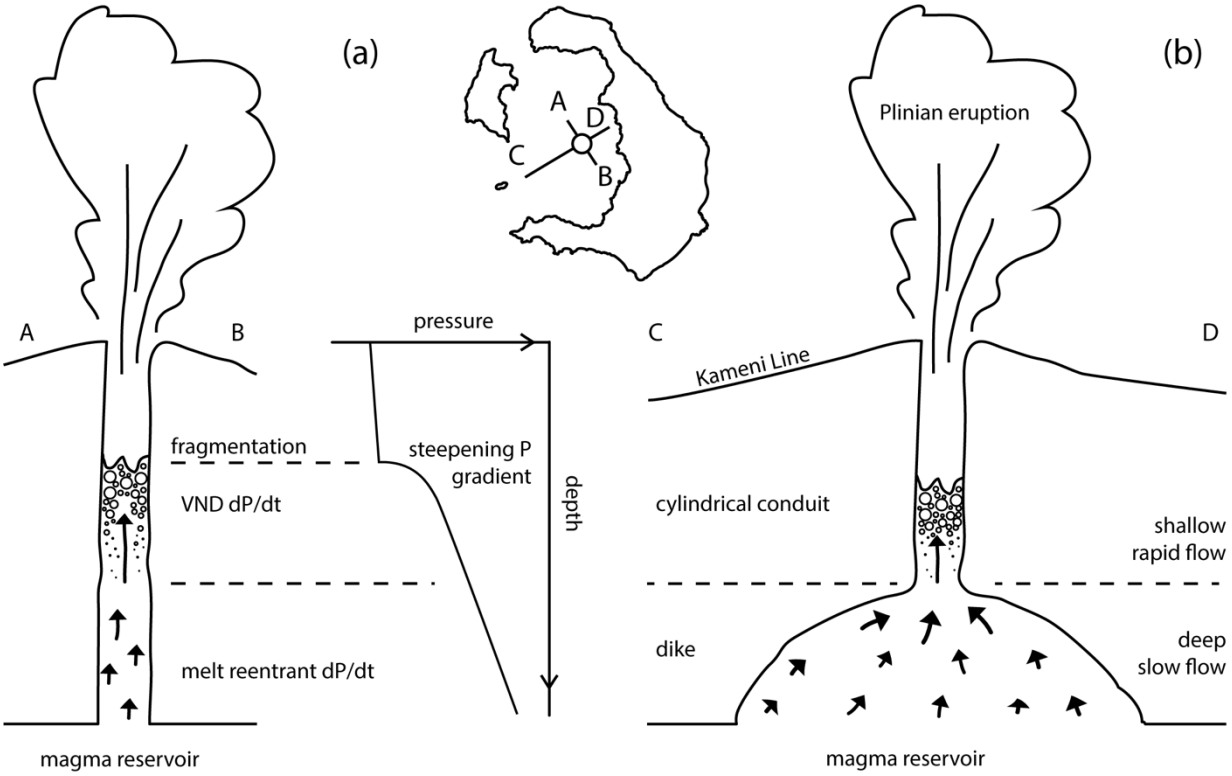
(a)
A
D
C
B
A
B
pressure
fragmentation
steepening P
gradient
VND dP/dt
depth
melt reentrant dP/dt
magma reservoir
(b)
Plinian eruption
C
D
Kameni Line
cylindrical conduit
shallow
rapid flow
dike
deep
slow flow
magma reservoir

Fig. 8

Tables (1-3)

Table 1:

Layer	Characteristics	Plume Height (km)*[1]	Wind Direction	MER (kg/s)[2]	MER (kg/s)[3]
P0	Coarse ash fall with some microphenocryst-rich pumices. Beds A of Cioni et al. (2000)	8.5 ± 1.5 [4]	S	$1.7 \pm 1.2 \times 10^6$	1.0×10^6
P1a1	Lapilli pumice fall with abundant microphenocryst-rich pumices. Reversely graded. Gray coloring.	11.6 ± 2.1	SSE	$5.8 \pm 3.9 \times 10^6$	3.7×10^6
P1a2	Lapilli pumice fall with abundant microphenocryst-rich pumices. Two reversely zoned layers. Gray coloring.	14.3 ± 1.1	SE	$1.3 \pm 0.4 \times 10^7$	8.8×10^6
P1b1	Pumice fall deposit with whiter appearance. Microphenocryst-rich pumices scarce.	18.0 ± 1.3	E	$3.4 \pm 1.1 \times 10^7$	2.3×10^7
P1b2	Pumice fall deposit with white appearance. Microphenocryst-rich pumices scarce. P1b1/P1b2 boundary marked by incoming of rare cauliform andesitic scoria.	28.4 ± 1.0	NE	$2.1 \pm 0.6 \times 10^8$	1.5×10^8
P1d	Following pyroclastic surge deposit (P1c), final pumice fall layer before passage to P2.	21.7 ± 1.1	No Wind ?	$7.2 \pm 1.3 \times 10^7$	5.0×10^7

*The plume height presented is determined using the 3.2 cm isopleth, assuming a lithic density of 2500 kg/m^3, and calculated using the plume inversion model of Carey and Sparks (1986), except for P0, where we used the value of Cioni et al. (2000). For each layer, the minimum and maximum plume height was determined based on uncertainties in the cross and downwind ranges; the average of this range is presented here along with the estimated uncertainty. Mass Eruption Rate (MER) was estimated using the methods of Wilson and Walker (1987) and Mastin et al. (2009), and the uncertainty estimated for the Wilson and Walker (1987) value. [1] Carey and Sparks (1986); [2] Wilson and Walker (1987); [3] Mastin et al. (2009); [4] Cioni et al. (2000).

Table 2:

Sample	Location	Fall Layer	Average Vesicle Diameter (μm) [a]	N_V (mm^{-3})	N_V [b] corrected (mm^{-3})	N_V [c] uncertainty (mm^{-3})	dP/dt [c] Heterog (MPa/s)	dP/dt [c] Homog. (MPa/s)
P0	Location 1	P0	13	6.24×10^5	2.50×10^6	7.58×10^5	2	50
RDP18	Location 1	P1a1	12	6.43×10^6	2.57×10^7	1.26×10^7	11	240
RDP20	Location 1	P1a2	4	1.45×10^7	5.78×10^7	9.04×10^6	17	420
RDP14	Location 11	P1b1/P1b2	9	5.37×10^6	2.15×10^7	5.94×10^6	9	220
RDP13	Location 11	P1b2	7	1.07×10^7	4.28×10^7	1.68×10^7	15	340
RDP11	Location 11	P1b2	5	1.64×10^7	6.56×10^7	1.50×10^7	19	450
RDP7	Location 11	P1b2	8	1.56×10^7	6.26×10^7	1.77×10^7	19	440
RDP5	Location 11	P1d	9	3.42×10^6	1.37×10^7	4.16×10^6	7	160

[a] Vesicle diameter is an average of the two axes.
[b] Vesicle Number Density (N_V) is corrected based on a vesicularity of 75%, taken from Wilson and Houghton (1990).
[c] N_V uncertainty is based on the 1 sigma SD of the Nv determined by analyzing each 500x image individually.
[d] Magma decompression rates (dp/dt) were calculated from N_V using the equations from Toramaru (2006), using assumptions of both heterogenous and homogenous nucleation.

Table 3:

Melt Reentrant Name	Fall Layer	Length of Melt Reentrant (μm)	H_2O Interior (wt.%)	CO_2 Interior (ppm)	Interior Pressure (MPa)	H_2O Mouth (wt.%)	CO_2 Mouth (ppm)	Pressure Mouth (MPa)	dP/dt Best fit (MPa/s)	dP/dt uncertainty (MPa/s)	Ascent Rate (m/s)	Best Fit Fragmentation Pressure (MPa)
Po-1	Po	220	3.8	0	110	2.8	0	65	0.025	0.02	1.17	50
RDP18-1	P1a1	90	4.3	0	119	2.9	0	61	0.25	0.1	11	40
RDP18-2	P1a1	160	4.3	0	119	1.5	0	18	0.14	0.05	4.9	10
RDP20-1	P1a2	180	3.4	0	80	1.4	0	16	0.04	0.02	1.5	20
RDP14-4	P1b1	320	3.2	0	72	2.31	0	40	0.008	0.001	0.3	30
RDP13-1	P1b2	80	2.9	0	60	2.6	0	50	0.012	0.02	0.56	50
RDP13-5	P1b2	80	1.9	0	28	1.67	0	23	0.01	0.01	0.37	20
RDP11-6	P1b2	110	4.2	0	115	3.3	0	76	0.1	0.1	6.3	80
RDP7-5	P1b2	140	4.3	0	119	3.8	0	97	0.02	0.02	1.43	90
RDP5-1	P1d	170	3.8	0	97	2.8	0	57	0.035	0.01	1.79	60
RDP5-2	P1d	90	2.4	0	43	1.8	0	26	0.035	0.01	1.3	20

Click here to access/download

Supplementary Material

Supplemental Tables Decompression DEC 2020.xlsx